Characterization of the Hot Deformation Behavior and Microstructure Evolution of a New γ-γ' Strengthened Cobalt-Based Superalloy

B. NITHIN, K. CHATTOPADHYAY, and G. PHANIKUMAR

Recently, cobalt-based γ-γ' microstructured superalloys have attracted attention. However, studies on their processing behavior [*i.e.*, processing maps (the variation of strain rate sensitivity (m) with temperature)] are limited. Thus, the high-temperature flow behavior of a γ-γ' Co-30Ni-10Al-5Mo-2Ta-2Ti-5Cr (at. pct) superalloy was investigated using isothermal compression tests between 1348 and 1498 K at strain rates from 0.001 to 10 s^{-1}. The m contour map was generated using the experimental flow stress values, which were used to locate the optimum hot workability and desired microstructural processing range. A strong dependence of m on the deformation parameters (temperature, strain rate, and strain) was observed. A maximum m value of around 0.3 at 1460 K to 1498 K and strain rates of 0.01 to 0.5 s^{-1} was found. The deformed samples show a fully recrystallized microstructure at high m. Unstable domains showed the formation of cavities at the grain boundary triple points and cracks along the grain boundaries at high strain rates (1 to 10 s^{-1}), corresponding to $m < 0.10$. A constitutive model was developed using an Arrhenius hyperbolic sine function, yielding an apparent activation energy of 540 ± 30 kJ mol^{-1} for hot deformation. This study indicates reasonable formability under certain conditions below the solvus, thus opening possibilities for further thermomechanical treatment.

I. INTRODUCTION

SUPERALLOYS are high-temperature structural materials mainly used in land-based and aircraft turbine engine components such as discs, blades, rotating shafts, nozzle guide vanes, and combustor liners.[1,2] For the fabrication of these critical components with the desired microstructural and mechanical properties, the alloys must undergo several crucial hot deformation processes.[3,4] At high temperatures, the flow behavior of these metallic alloys is complex and sensitive to thermomechanical parameters such as the temperature, strain rate, and strain.[5] Thus, during high-temperature deformation, it is essential to control the thermomechanical parameters to achieve the required properties. Work hardening and softening (dynamic recovery and recrystallization) mechanisms are the two dominant metallurgical phenomena that occur during the high-temperature deformation process.[6] Thus, it is important to characterize and understand the dynamic recrystallization behavior of these alloys, which refines the coarse grains and affects the flow stress during hot deformation.

Superalloys based on cobalt have applications as critical turbine engine parts, where hot corrosion, wear, and oxidation resistance are required.[7–9] Some of the most widely used commercial cobalt alloys such as Haynes 188, stellite, and MAR-M are strengthened by the use of solidsolutions and metallic carbides.[10,11] These alloys possess good resistance to oxidation and hot corrosion. The strength values at high temperatures are inadequate compared to nickel-based superalloys, which derive their strength from their γ-γ' microstructure. Recently, it was shown that the formation of a γ-γ' microstructure in cobalt-based alloy systems (Co-Al-W and Co-Al-Mo-Nb/Ta-based alloys) could overcome this drawback, enabling the development of high-strength, high-temperature cobalt-based superalloys.[12,13] Significant developments have been made in the design of new alloys by adding a solute to improve the oxidation/corrosion resistance, thermal stability, high-temperature mechanical properties, and reduction of the density of the Co-Al-W base alloys.[14–23] Various superalloy development strategies can be used to

---

B. NITHIN and G. PHANIKUMAR are with the Department of Metallurgical and Materials Engineering, Indian Institute of Technology Madras, Chennai, Tamil Nadu 600036, India. Contact e-mail: nithinbaler@gmail.com K. CHATTOPADHYAY is with the Department of Materials Engineering, Indian Institute of Science, Bangalore, Karnataka 560012, India.

improve the high-temperature properties of Co-Al-Mo-Nb/Ta-based alloys, and some of these alloys show superior high-temperature properties to nickel-based superalloys.[24–26] One among these is a newly developed alloy with a base composition of Co-30Ni-10Al-5Mo-2Ta-2Ti, which was obtained after a series of experiments. With a view towards improving the properties at high temperatures, systematic Cr addition (2, 5, 8, and 10 at. pct) to the base composition has been studied.[27] In these alloys, the L_{12} ordered γ' precipitates with stoichiometry $(Co,Ni)_3(Al,Ta,Ti,Mo,Cr)$ are distributed in a disordered face-centered cubic (FCC) cobalt matrix. Out of these series of alloys, the alloy with a composition Co-30Ni-10Al-5Mo-2Ta-2Ti-5Cr has a solvus temperature of 1378 K and a yield strength greater than 560 MPa at 1143 K. This is comparable to those of a few existing cobalt-based superalloys and commercially available nickel-based superalloys. The strengthening of the present alloy at high temperature is mainly due to the presence of γ' precipitates in the FCC cobalt matrix. Conventionally, most nickel-based superalloys are processed above the solvus temperature to avoid the γ' precipitate strengthening effect. The present alloy of interest contains a high concentration of alloying elements, such as Al, Cr, Ti, Ta, and Mo, which makes hot forming challenging. Unlike nickel-based superalloys, the gap between the melting point and the solvus for the cobalt-based superalloys is wide.

The generation of strain rate sensitivity contour maps[28–33] and processing maps using the dynamic material model (DMM)[34–36] has been widely used to optimize the processing parameters and, thus, control the alloy microstructure during high-temperature deformation. However, there are limited studies concerning the high-temperature deformation behavior of cobalt-based alloys,[37–39] which are strengthened by formation of a solid solution, and none concerning γ-γ' cobalt-based superalloys. In this present study, the hot deformation behavior of a W-free γ'-strengthened cobalt-based superalloy has been investigated by isothermal uniaxial compression tests over a wide range of deformation temperatures and strain rates. Based on the experimental results, a strain rate sensitivity (m) contour map was generated, and the correlation with the deformation microstructures has been studied in detail.

II. MATERIALS AND METHODS

The nominal chemical composition of the alloy used in this study and the composition measured using an energy dispersive X-ray spectroscope (EDS) attached to a field-emission electron probe microanalyzer (EPMA, JEOL) are given in Table I. The alloy was prepared in the form of a slab (200 mm × 150 mm × 30 mm) using vacuum arc melting, and subsequently, it was subjected to hot isostatic pressing to ensure the elimination of micro-pores. Cylindrical samples with a diameter and height of 7 and 10.5 mm, respectively, were cut from the slab using electrical discharge machining (EDM). Then,

Table I.   The Composition (Atomic Percentage) of Various Elements in the Cobalt-Based Alloy Under Study

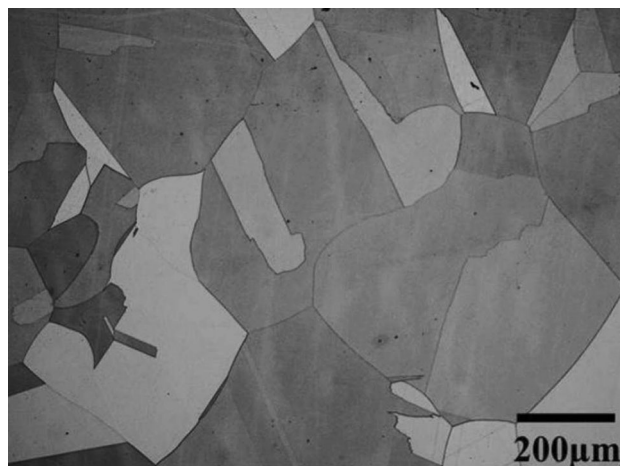| Elements	Nominal Composition	Actual Composition
Co	46	46.73 ± 0.19
Ni	30	29.96 ± 0.23
Al	10	9.54 ± 0.47
Mo	5	4.95 ± 0.2
Ta	2	1.91 ± 0.02
Ti	2	2.13 ± 0.22
Cr	5	4.78 ± 0.05

Fig. 1—Optical microstructure of the Co-30Ni-10Al-5Mo-2Ta-2Ti-5Cr alloy after solution treatment at 1523 K for 2 h air cooled.

the machined samples were solutionized at 1523 K for 2 hours. Isothermal uniaxial compression tests were carried out at temperatures of 1348 K, 1398 K, 1448 K, and 1498 K and strain rates of 0.001, 0.01, 0.1, 1, and 10 s^{-1} in a thermomechanical simulator (Gleeble 3800). Nickel paste and graphite foils were used at the interface between the sample and tungsten carbide anvils to minimize friction. All specimens were heated to deformation temperature at a rate 5 K s^{-1} and soaked for 600 seconds. After achieving a required true strain of 0.7, the samples were quenched in water to arrest the deformation of the microstructure. The deformed samples were cut parallel to the compression axis for microstructural studies. For optical microscopy, the cut surface was mechanically polished and etched for 60 seconds in a solution of 10 g $CuSO_4$, 50 mL HCl, and 50 mL distilled water at room temperature (303 K). For electron backscatter diffraction (EBSD) analysis, the cut samples were electropolished with a solution consisting of 10 pct perchloric acid in ethanol. A scanning electron microscope (SEM, Sirion XL30 FEG™ FEI) equipped with an EBSD detector was used for characterization. Figure 1 shows the optical microstructure of the studied alloy after solution treatment. The microstructure consists of coarse equiaxed grains with an average grain size of 400 ± 50 μm.
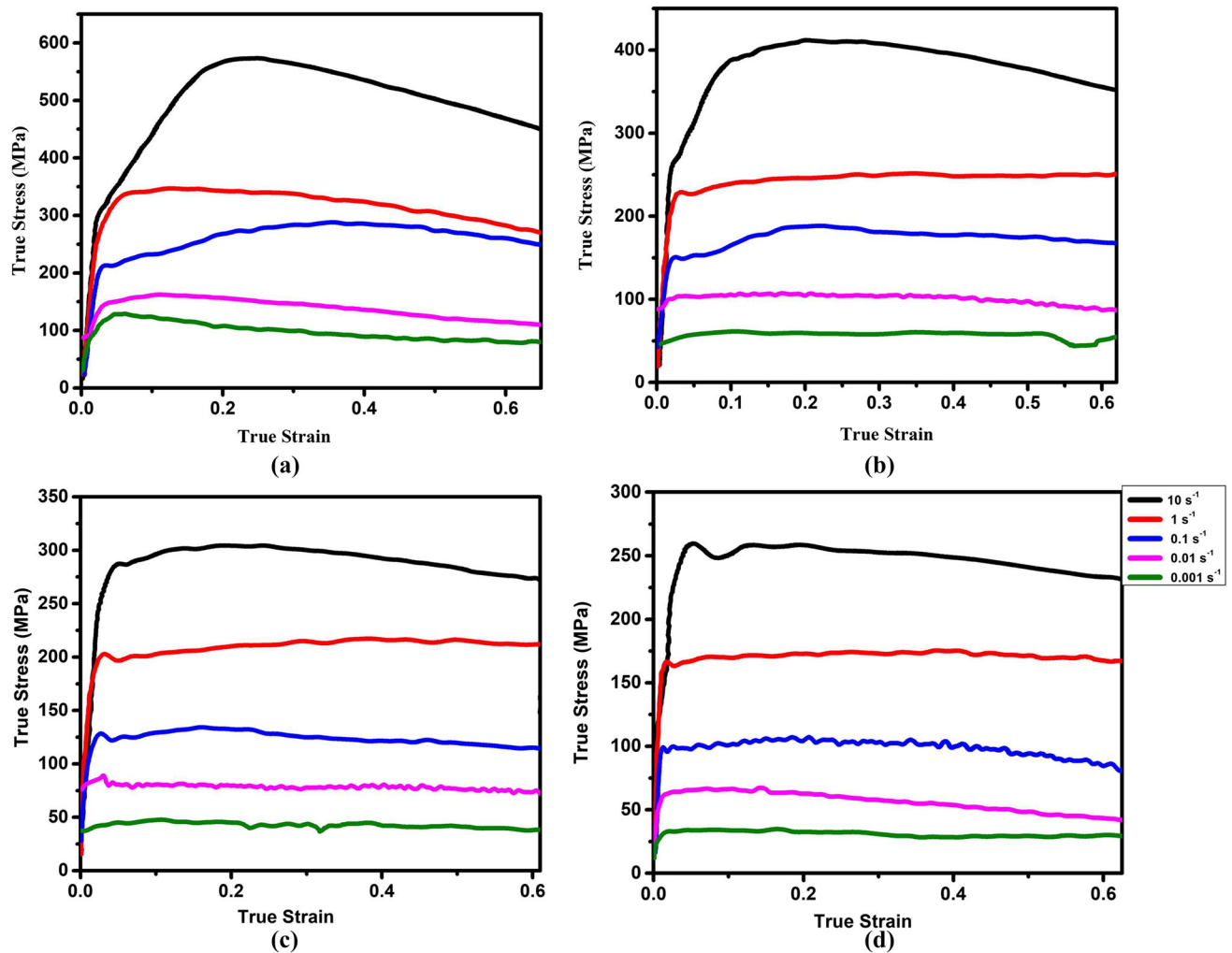
Fig. 2—True-stress-strain curves obtained at different deformation temperatures and strain rates (*a*) 1348, (*b*) 1398, (*c*) 1448, (*d*) 1498 K.

III. RESULTS

A. *True-Stress-Strain Curves*

The shape of the flow curves during high-temperature deformation depends on the microstructural evolution and is influenced by the temperature, strain rate, and strain. There are three stages in the flow curve: (1) work hardening to the peak stress, (2) softening, where the stress value decreases continuously, and (3) a steady state, where the stress value becomes constant with strain. The first stage, work hardening, is usually seen under all conditions. Depending on the deformation condition (T, $\dot{\varepsilon}$), the critical strain corresponds to the peak stress will change and is directly attributed to dislocation density. The second stage involves the formation of subgrains by rearrangement and the annihilation of dislocations (polygonization). This process is typically observed in materials with high stacking fault energies. In the third stage, the rate of dislocation density increases and the elimination of dislocations (softening) reaches equilibrium.

Figure 2 shows the true-stress-strain curves for the alloy deformed to a true strain of 0.7 at temperatures 1348 K, 1398 K, 1448 K, and 1498 K and strain rates of 0.001 to 10 s^{-1}. The flow stress is sensitive to both the deformation temperature and the strain rate. For a given temperature, the value of the flow stress increases with increasing strain rate. Similarly, the value of the flow stress increases with decreasing temperature at a constant strain rate. Two types of behavior can be observed in the true-stress-strain curve. The flow stress value reaches a peak at the initial stage of deformation, decreases gradually, and becomes stable with further deformation. This feature resembles the behavior of an alloy with low stacking fault energy and indicates the formation of dynamic recrystallization (DRX) grains.[6,40,41]

B. *Kinetic Analysis*

Hot deformation is a thermally activated process. The combination of temperature and strain rate affects the deformation behavior of the material. Sellars and
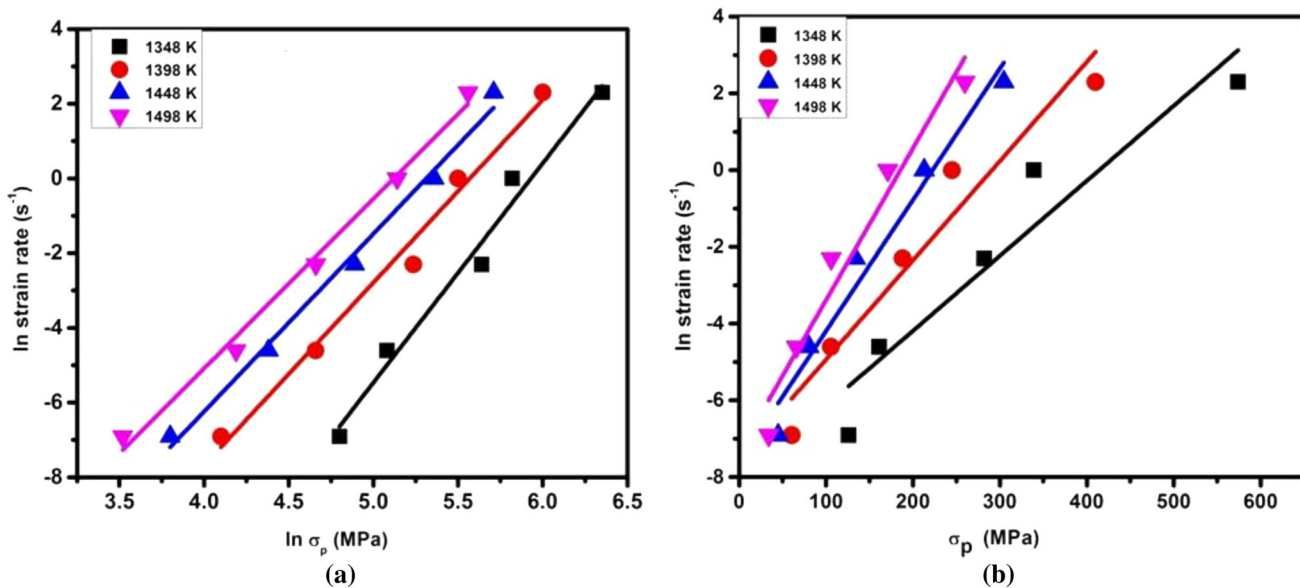
Fig. 3—(a) and (b) show variation of flow stress with strain rate at different test temperatures for the Co-30Ni-10Al-5Mo-2Ta-2Ti-5Cr alloy. The alloy was solutionized at 1523 K for 2 h and air cooled prior to test.

Tegart[42] proposed an equation to relate the dependence of the flow stress on the temperature and strain rate during hot deformation, shown in Eq. [1].

$$\dot{\varepsilon} = Af(\sigma)\exp\left(\frac{-Q}{RT}\right) \qquad [1]$$

Depending on the peak stress value, $f(\sigma)$ can be expressed as power law equation, exponential equation, or hyperbolic sine law, as shown in Eqs. [2] through [4].

$$f(\sigma) = \sigma^{n1} \quad [\text{for } \alpha\sigma < 0.8] \qquad [2]$$

$$f(\sigma) = \exp(\beta\sigma) \quad [\text{for } \alpha\sigma > 1.2] \qquad [3]$$

$$f(\sigma) = [\sinh(\alpha\sigma)]^n \quad [\text{for all } \alpha\sigma] \qquad [4]$$

Here, $n1$, A, β, α, and n are the material constants, where $\alpha = \beta/n1$, and σ is flow stress, which is taken as the peak stress for analysis. For deformation at higher strain rates or lower temperatures, a large strain is required to reach steady state stress. In general, the peak stress is considered for kinetic analysis. The present alloy exhibits a DRX type of flow curve, where the peak stress (σ_p) can be easily attained. The peak stress in the flow curve indicates the critical condition for DRX initiation.[43,44] Q is activation energy for the process (kJ mol^{-1}) and R is universal gas constant 8.314 J mol^{-1}K^{-1}.

To determine the material constants, the natural logarithm was taken on both sides after substituting Eqs. [2] and [3] into Eq. [1].

$$\ln\dot{\varepsilon} = \ln A + n1\ln\sigma - \frac{Q}{RT} \qquad [5]$$

$$\ln\dot{\varepsilon} = \ln A + \beta\sigma - \frac{Q}{RT} \qquad [6]$$

By taking the logarithm after substituting Eq. [4] into Eqs. [1], [7] was obtained.

$$\ln\dot{\varepsilon} = \ln A + n\ln[\sinh(\alpha * \sigma_p)] - \frac{Q}{RT} \qquad [7]$$

By differentiating the above equation with respect to temperature (T) at a constant strain rate, Eq. [8] was obtained, which can be used to calculate apparent activation energy of the process.

$$Q = nR\left[\frac{\partial\ln[\sinh(\alpha * \sigma_p)]}{\partial[\frac{1}{T}]}\right] \qquad [8]$$

At a constant deformation temperature, the values of $n1$ and β can be obtained by using the slopes of the $\ln\dot{\varepsilon}$ vs $\ln\sigma_p$ and $\ln\dot{\varepsilon}$ vs σ_p curves shown in Figure 3. The average values of $n1$ and β were found to be 5.01 and 0.03, respectively. The value of α can be calculated using the relationship $\alpha = \frac{\beta}{n1}$ and was found to be 0.006.

The stress exponent 'n' can be obtained from the slope of the $\ln\dot{\varepsilon}$ vs $\ln[\sinh(\alpha * \sigma_p)]$ curve shown in Figure 4. The average value of n is determined to be 3.57.

The plots of $\ln[\sinh(\alpha * \sigma_p)]$ vs $[\frac{1}{T}]$ at each strain rate are shown in Figure 5. Q was obtained by calculating

the slope of the $\ln\left[\sinh\left(\alpha * \sigma_p\right)\right]$ vs $\left[\frac{1}{T}\right]$ curve and substituting it into Eq. [8]. The apparent activation energy was found to be 540 ± 30 kJ mol^{-1}. The calculated apparent activation energy for the studied alloy is higher than the self-diffusion of pure cobalt (250 kJ mol^{-1}).[45] This indicates that DRX is the dominant softening mechanism. This is similar to the case of some titanium alloys and nickel-based superalloys.[46,47]

Based on the experimental results, a constitutive equation describing the dependence of the flow stress with the strain rate and deformation temperature of the alloy was determined (see Eq. [9]).

$$\dot{\varepsilon} = 3.75 * 10^{18}[\sinh(0.006 * \sigma_p)]^{3.569}\exp\left(\frac{-540 * 10^3}{RT}\right)$$
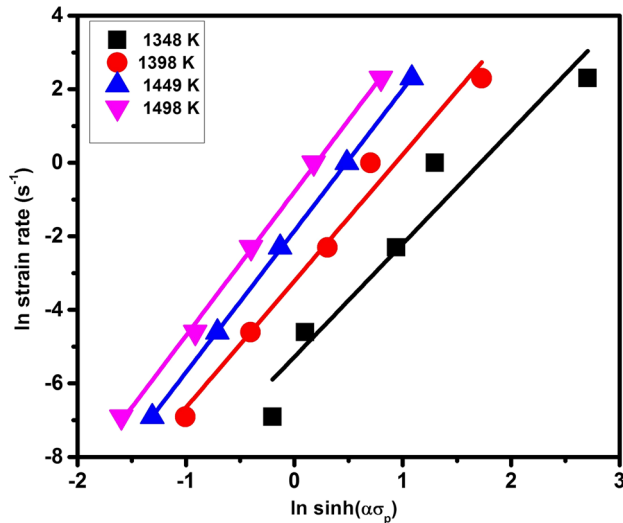[9]

Fig. 4—The relation between flow stress and strain rate at different temperatures for the Co-30Ni-10Al-5Mo-2Ta-2Ti-5Cr alloy.
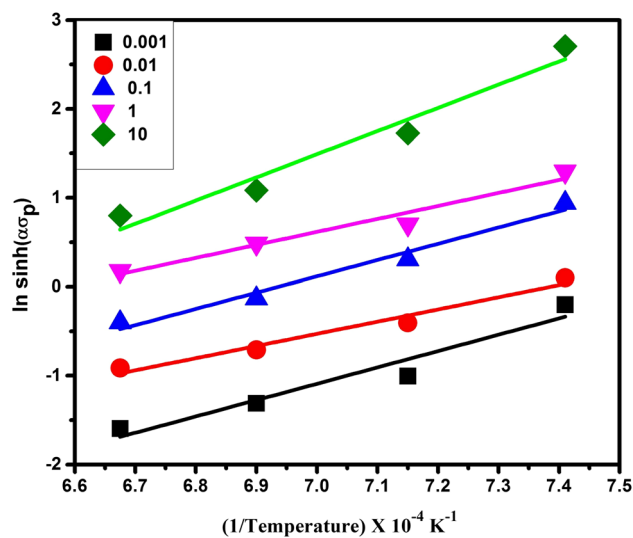

Fig. 5—Variation of flow stress with deformation temperature at different strain rates for the Co-30Ni-10Al-5Mo-2Ta-2Ti-5Cr alloy.

The strain rate and deformation temperature can be expressed by the Zener–Hollomon parameter,[6] which can be used to evaluate the validity of the developed constitutive equation; this is expressed by Eq. [10]

$$Z = \dot{\varepsilon}\exp\left(\frac{Q}{RT}\right) = A[\sinh(\alpha * \sigma)]^n$$
[10]

The variation of Zener–Hollomon parameter (Z) with peak stress (σ_p) is shown in Figure 6. The correlation coefficient for linear regression is 0.967. It can be seen that peak stress increases with increasing Zener–Hollomon parameter.

C. *Strain Rate Sensitivity*

The strain rate sensitivity is an important parameter to identify the safe working domain during hot working. To correlate the microstructure developed after 50 pct deformation with the strain rate sensitivity map, the stress values at 0.6 strain at different temperatures and strain rates were used to calculate the strain rate sensitivity values. In contrast, in kinetic analysis, the peak stress is used. For deformation at higher strain rates or lower temperatures, a large strain is required to reach steady state stress; thus, the peak stress represents the critical condition for DRX nucleation. The stress values at different strain rates were interpolated using a cubic spline. The derivative of the spline fit gives the strain rate sensitivity parameter (m).

$$m = \left(\frac{\partial \ln \sigma}{\partial \ln \dot{\varepsilon}}\right)_{T,\varepsilon}$$
[11]

Figure 7(a) shows the contours of the strain rate sensitivity at a different temperatures and strain rates. Two separate regimes can be seen in the map, one with $m < 0.1$ at strain rate > 1 s^{-1} at all temperatures and
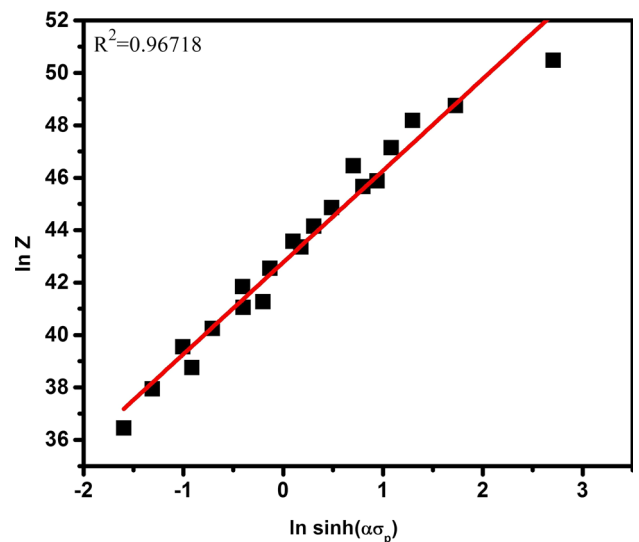

Fig. 6—The relation between hot deformation peak stress and Z parameter of the studied alloy.

other with $m \geq 0.2$, which indicate that the mechanism varies with deformation conditions.

D. Instability Map

The instability parameter as per the Ziegler instability criterion[48] is calculated by using the value of m. It is based on the principle of the maximum rate of entropy production during plastic flow, which is given by the following equation.

$$\xi(\dot{\varepsilon}) = \frac{\partial \ln\left[\frac{m}{(m+1)}\right]}{\partial \ln \dot{\varepsilon}} + m < 0 \qquad [12]$$

The variation of $\xi(\dot{\varepsilon})$ plotted as a function of temperature and strain rate gives the instability map.

The region where $\xi(\dot{\varepsilon})$ is negative represents the flow instabilities or inhomogeneous deformation (material flow). Adiabatic shear bands, wedge cracking, intercrystalline cracking, cavitation, and flow localization are the characteristic features of the flow instabilities observed in the microstructures. The instability map at a true strain of 0.6 is shown in Figure 7(b).

E. Processing Map

Use of a processing map based on the DMM is another way to identify the optimum regime for carrying out thermomechanical processing. The specific principle has been discussed elsewhere.[34] A processing map gives the response of a material and associated mechanism during deformation. The map for the Co-30Ni-10Al-5Mo-2Ta-2Ti-5Cr alloy was generated at a true strain of
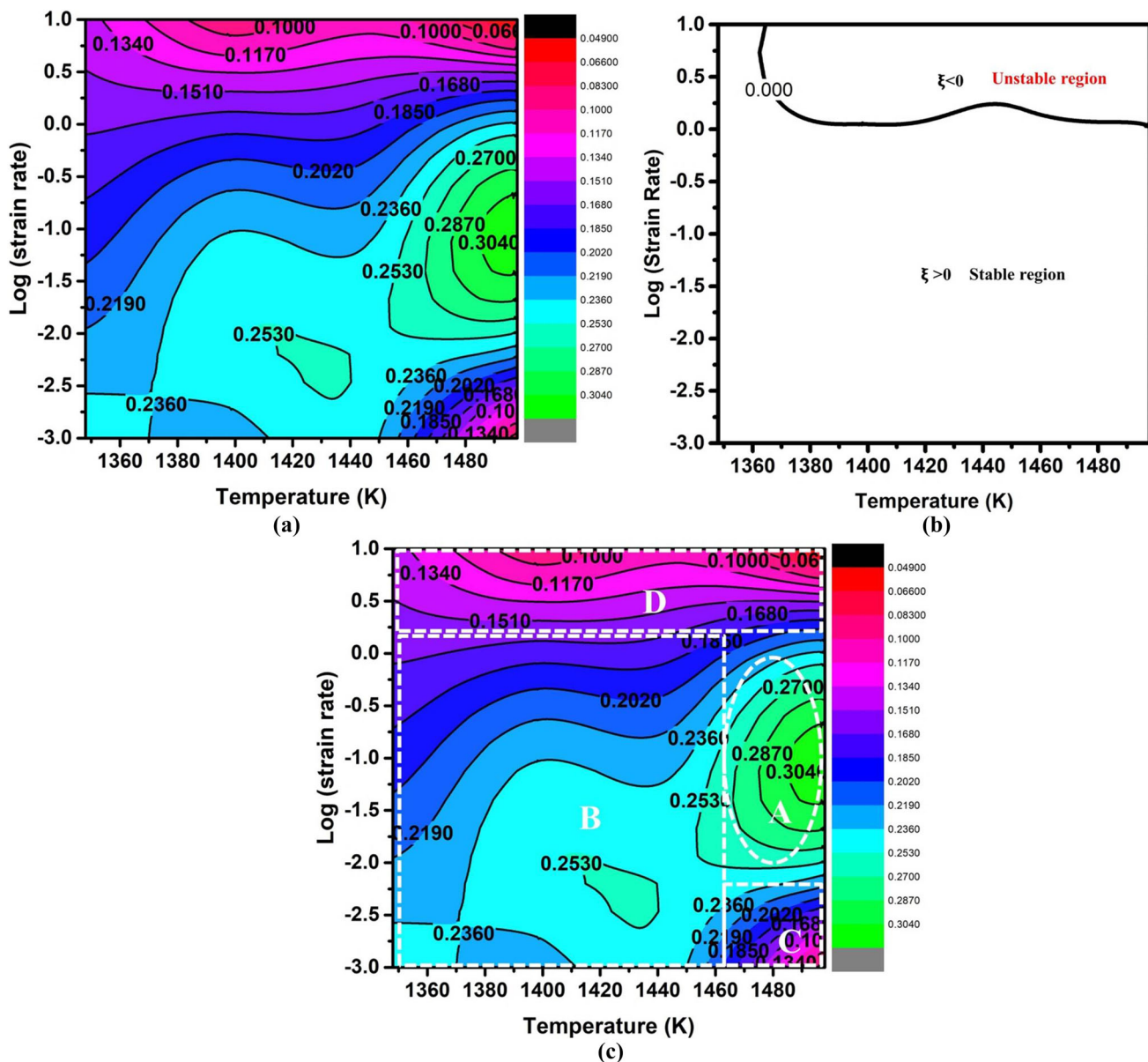

Fig. 7—(a) Strain rate sensitivity contour map at 0.6 strain, (b) instability map, (c) different domains in the strain rate sensitivity map. The maps are generated for solution treated at 1523 K for 2 h and air cooled alloy having a composition Co-30Ni-10Al-5Mo-2Ta-2Ti-5Cr (at. pct).

0.6 by superimposing the power dissipation map and instability map on the temperature and logarithmic strain rate frame. The contours in the map represent the efficiency of power dissipation and its dependency on the deformation parameters such as temperature and strain rate, as shown in Figure 8. The bold dark line divides the map into a stable $(\xi(\dot{\varepsilon}) > 0)$ and unstable domains $(\xi(\dot{\varepsilon}) < 0)$. In the stable domain, softening mechanisms, such as dynamic recovery and dynamic recrystallization, will occur. Thus, hot deformation should be carried out in this domain. In unstable or unsafe domains, flow instabilities, such as grain boundary cracking, shear bands, and cavities, will occur during processing. This region should be avoided during deformation. The optimum hot workability is determined in the stable (safe) domain with the highest power dissipation efficiency, where nearly fully dynamic recrystallization can be identified.

IV. DISCUSSION

A. Flow Behavior

The characteristics of the flow curve shown in Figure 2 are related to the competing phenomena of work hardening and softening. In the initial stages of deformation, there is an increase in the flow stress which can be attributed to dislocation interaction and multiplication. Here, work hardening is the dominant phenomena. With further deformation, the dislocation density starts to increase and reaches a threshold that results in the nucleation of DRX grains. This phenomenon (softening) can be seen from the decrease in the stress value in the flow curve. At larger strains, the flow stress stabilizes, which reflects the dynamic equilibrium between the work hardening and softening.
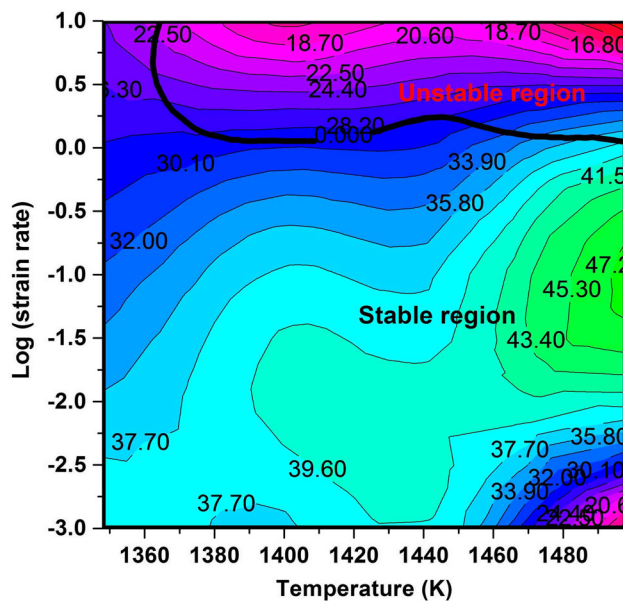

Fig. 8—Processing map at 0.6 strain. The map is generated for solution treated at 1523 K for 2 h and air cooled alloy having a composition Co-30Ni-10Al-5Mo-2Ta-2Ti-5Cr (at. pct).

B. Deformation-Induced Microstructural Evolution

The strain rate sensitivity map is consistent with the processing map, conveying essentially the same information. Depending on the microstructural evolution and m value, the contours of strain rate sensitivity map can be divided into four domains as shown in Figure 7(c).

Domain A lies in the temperature and strain rate range of 1460 K to 1498 K and 0.01 to 0.5 s^{-1}, respectively. The strain rate sensitivity value is ca. 0.3 in this domain. The deformed microstructure of this domain is shown in Figures 9(a) and (b). It can be seen that prior grains are almost fully replaced by uniform equiaxed grains. The presence of curved or serrated grain boundaries in the deformed microstructure indicates the formation of DRX grains, and the high value of m indicates that DRX is the dominant mechanism. Alloys of cobalt with nickel are known to exhibit lower stacking fault energies.[49] Thus, the studied alloy behaves like a low stacking fault energy material. The DRX grains form mainly along the pre-existing grain boundaries by the grain boundary bulging mechanism. This occurs because of the difference in the dislocation density along the adjacent grain. Thus, the nucleation mechanism of DRX for the present alloy during hot deformation belongs to the discontinuous dynamic recrystallization (DDRX) process.[50,51]

Domain B lies in a wide temperature range of 1345 K to 1448 K and a strain rate range of 0.001 to 1 s^{-1} with a strain rate sensitivity of 0.2 to 0.25. The microstructure in this domain consists of coarse deformed grains that are elongated perpendicular to the compression axis. A small fraction of DRX grains nucleated along the pre-existing grain boundaries, exhibiting a typical necklace-like structure, as shown in Figure 9(c). Because of the lower deformation temperature, partial dynamic recrystallization has occurred in this domain. At a particular strain rate, m increases with increasing deformation temperature. Because of the coarse initial grains, a larger true strain is necessary to complete the DRX process.

Domain C lies in the temperature range of 1470 K to 1498 K at a strain rate of 0.001 s^{-1} with an m value of 0.1 to 0.13. The microstructure consists of the coarse equiaxed DRX grains shown in the Figure 9(d). Because this domain covers a high temperature (1470 to 1498 K) and low strain rate (0.001 to 0.005 s^{-1}) range where solute drag effects are negligible, there is higher grain boundary migration, where grain growth is the dominant mechanism in this region.[52–54]

Domain D falls in the unstable region of the instability map. This region can be seen at high strain rates (>1 s^{-1}) and a temperature range of 1398 K to 1498 K, i.e., $m < 0.1$. Grain boundary cracking, cavity, adiabatic shear bands, and localized plastic flow are the characteristic features observed in the unstable domain. For validation, microstructural analysis of the deformed samples in this region is carried out. Figures 9(e) and (f) show the optical microstructure of the flow instability of the studied alloy deformed at 1398 K and 1498 K and a strain rate of 10 s^{-1}. The microstructure clearly shows
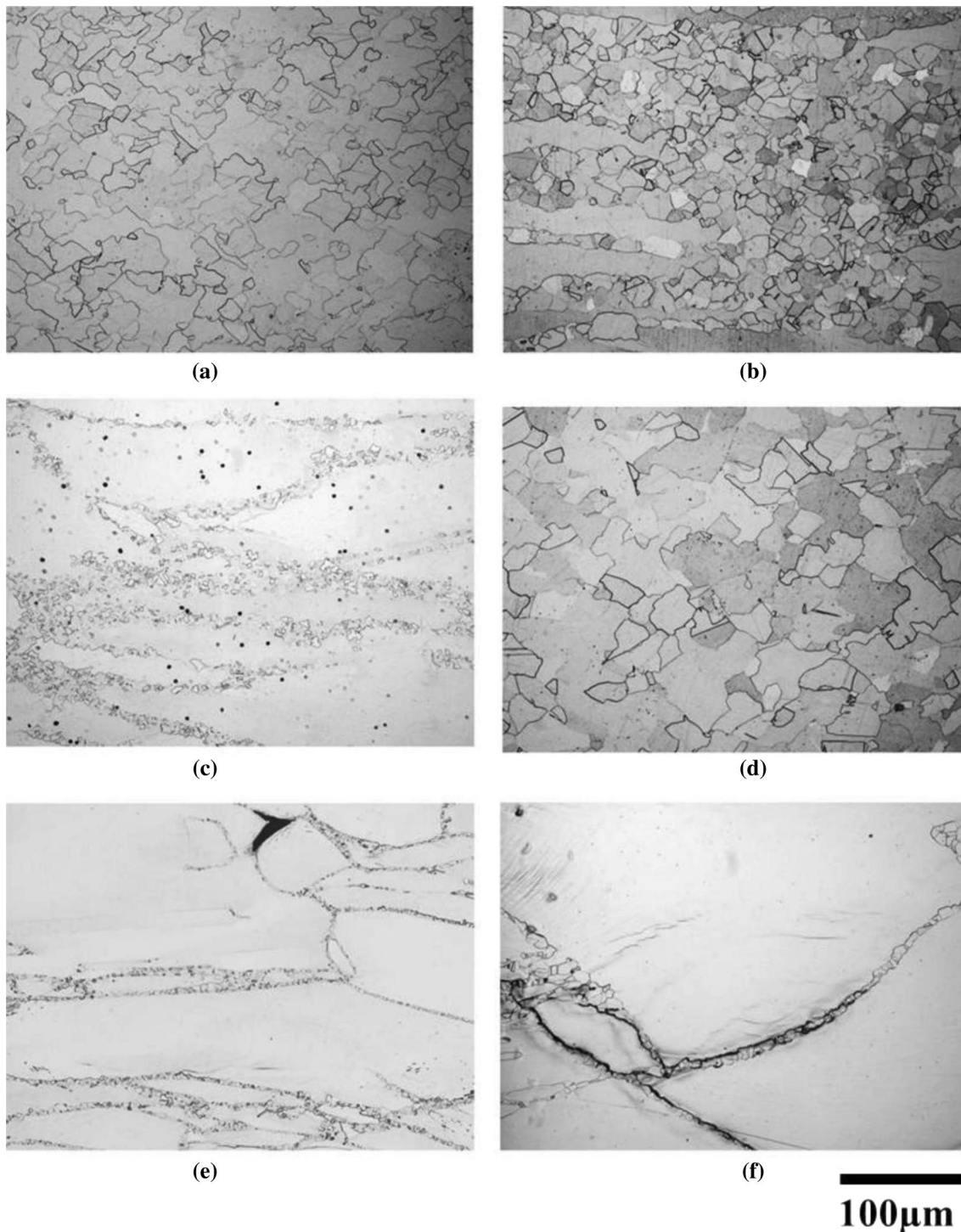
Fig. 9—The figure shows representative optical microstructure of deformed samples obtained from the different domains of the strain rate sensitivity map (*a*) and (*b*) Domain A, (*c*) Domain B, (*d*) Domain C, (*e*) and (*f*) Domain D as shown in the map.

the formation of cavities or cracks at the grain boundary triple points, and the occurrence of cracks along the grain boundaries indicates the inhomogeneous flow behavior of the material. The observed cracks likely arise from incipient melting and intergranular embrittlement. Some studies have reported similar observations in commercially available superalloys.[46,55] This region should be avoided during hot working.

It is essential to compare the processing map of the present alloy and associated mechanisms with commercially available cobalt-based superalloys such as Haynes 188, Co-Cr-Mo-N, and some of the nickel-based superalloys. The hot deformation behavior of the present alloy is different from the current cobalt-based superalloys. The stable regime for processing the present alloy was found below a strain rate of 1 s^{-1} at all
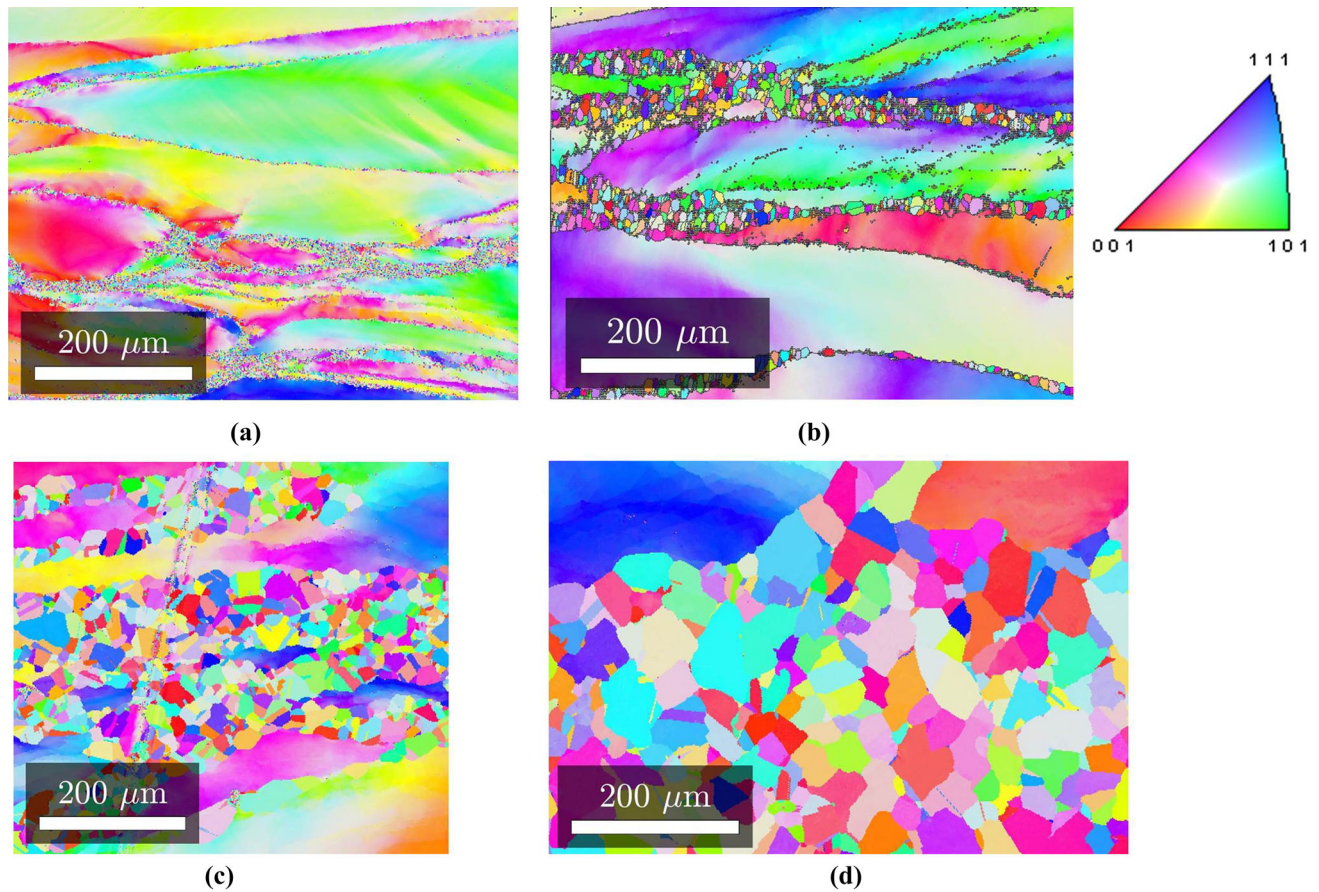
Fig. 10—Map of the inverse pole figure (IPF) of the present alloy deformed to a true strain 0.7 and strain rate 0.1 s^{-1} at different temperatures (*a*) 1348, (*b*) 1398, (*c*) 1448, (*d*) 1498 K.

temperatures, whereas, for other cobalt-based superalloys, such as Co–28Cr–6Mo–0.16N and Co–30Ni–21Cr–10Mo, the stable regimes occur at strain rates greater than 1 s^{-1}.[39,56] The processing map of Haynes 288 shows the unstable regime in the high strain rate (> 1 s^{-1}) region and the DRX regime at lower strain rates and higher temperatures.[57] This is similar to the processing map reported by us. For both alloys, fine equiaxed DRX grains were identified, corresponding to deformation at a strain rate of 0.05–0.5 s^{-1} and temperature range of 1448 K to 1498 K. However, the hot deformation map of Inconel 690 is different from that of the present alloy.[58] The deformation map of Inconel 690 contains two stable domains: one in the temperature range 1243 K to 1393 K at strain rates of 0.03 to 3.3 s^{-1} and the other in the temperature range of 1423 to 1473 K at strain rates of 0.003 to 0.1 s^{-1}. The unstable deformation domain was found at temperatures lower than 1313 K and strain rates higher than 0.56 s^{-1}. Complete DRX was seen in the sample deformed in the two stable regions, whereas flow instabilities, such as shear bands and inhomogeneous flow, were identified in the unstable domain. The difference in behavior is due to the different alloying elements and initial microstructure.

C. *Effect of Deformation Temperature on Microstructure Evolution*

Figure 10 shows the EBSD maps of the grain structures of the sample deformed at a true strain of 0.7 at a constant strain rate and different temperatures. The deformed microstructures are dependent on the processing temperature. Figure 10(a) shows the microstructure of the sample deformed at low temperature (1348 K). It consists of heavily deformed original grains and a small fraction of new grains with an average grain size of 1.5 μm, which are nucleated along the initial grain boundaries. The curved or wavy structure indicates the formation of DRX grains. When the deformation temperature was increased to 1398 K to 1448 K, equiaxed DRX grains with an average grain size of 3 μm at 1398 K and 26 μm at 1448 K started to form. These, along with deformed initial grains, are shown in Figures 10(b) and (c). A necklace-like structure under these conditions was also observed. Material with low stacking fault energies usually shows this type of behavior, where the dynamic recovery is slow, hindering dislocation climb and cross-slip.[59] As a result of the slow recovery process, the dislocation density increases to a critical value. This is necessary for the initiation of

the dynamic recrystallization process, where DRX grains form along the pre-existing grain boundaries. Thus, the original grains were completely replaced by the uniform equiaxed DRX grains with an average grain size of 60 μm on deformation at 1498 K, as shown in Figure 10(d). The above observations indicate that the fraction of DRX grains increases with increasing deformation temperature. The high temperature reduces the critical density of dislocation required for dynamic recrystallization nucleation. The DRX grains are also larger at higher temperatures because the grain boundary mobility increases with increasing deformation temperature.

V. CONCLUSION

The present work establishes the hot workability of a new W-free cobalt-based γ-γ' strengthened superalloy containing molybdenum and tantalum. Isothermal hot compression tests of the Co-30Ni-10Al-5Mo-2Ta-2Ti-5Cr alloy were carried out in the temperature range of 1348 K to 1498 K and at strain rates of 0.001 to 10 s^{-1}. A strain rate sensitivity map was generated, and the corresponding microstructures were investigated. The conclusions can be summarized as follows:

(1) The optimum hot working regime (high m value of ca. 0.3) was found between 1460 K and 1498 K at strain rates of 0.001 to 0.5 s^{-1}. The deformed microstructure in this domain contains dynamically recrystallized grains.

(2) Unstable regions were found at high strain rates (> 1 s^{-1}), which were characterized by the formation of cavities and the occurrence of grain boundary cracking in the deformed samples. This region should be avoided during the hot deformation process.

(3) A constitutive equation was developed using the peak stress, and the calculated apparent activation energy, 540 ± 30 kJ mol^{-1} is consistent with those of some existing nickel and cobalt-based super alloys. The equation is as follows:

$$\dot{\varepsilon} = 3.75 * 10^{18} \sinh(\alpha * \sigma_p)]^{3.569} \exp\left(\frac{-540 * 10^3}{RT}\right).$$

REFERENCES

1. A. S. M. International Handbook Committee, ASM Int. 1, 1993.
2. R.C. Reed: *The Superalloys Fundamentals and Applications,* Cambridge, Cambridge University Press, 2006.
3. M.O. Alniak and F. Bedir: *Mater. Des.*, 2010, vol. 31, pp. 1588–92.
4. J.W. Brooks: *Mater. Des.*, 2000, vol. 21, pp. 297–303.
5. A. Dehghan-Manshadi, M.R. Barnett, and P.D. Hodgson: *Metall. Mater. Trans. A*, 2008, vol. 39, pp. 1359–70.
6. F.J. Humphreys and M.Hatherly: *Recrystallization and Related Annealing Phenomena,* 2004.
7. D. Coutsouradis, A. Davin, and M. Lamberigts: *Mater. Sci. Eng. A*, 1987, vol. 88, pp. 11–19.
8. D.L. Douglass, V.S. Bhide, and E. Vineberg: *Oxid. Met.*, 1981, vol. 16, pp. 29–79.
9. N. Eliaz, G. Shemesh, and R.M. Latanision: *Eng. Fail. Anal.*, 2002, vol. 9, pp. 31–43.
10. W.H. Jiang, X.D. Yao, H.R. Guan, and Z.Q. Hu: *J. Mater. Sci. Lett.*, 1999, vol. 8, pp. 303–05.
11. W.H. Jiang, X.D. Yao, H.R. Guan, and Z.Q. Hu: *J. Mater. Sci.*, 1999, vol. 4, pp. 2859–64.
12. J. Sato, T. Omori, K. Oikawa, I. Ohnuma, R. Kainuma, and K. Ishida: *Science*, 2006, vol. 312, pp. 90–91.
13. S.K. Makineni, B. Nithin, and K. Chattopadhyay: *Scr. Mater.*, 2015, vol. 98, pp. 36–39.
14. A. Bauer, S. Neumeier, F. Pyczak, and M. Göken: *Scr. Mater.*, 2010, vol. 63, pp. 1197–1200.
15. G. Feng, H. Li, S.S. Li, and J.B. Sha: *Scr. Mater.*, 2012, vol. 67, pp. 499–502.
16. F.B. Ismail, V.A. Vorontsov, T.C. Lindley, M.C. Hardy, D. Dye, and B.A. Shollock: *Corros. Sci.*, 2017, vol. 116, pp. 44–52.
17. L. Klein, A. Bauer, S. Neumeier, M. Göken, and S. Virtanen: *Corros. Sci.*, 2011, vol. 53, pp. 2027–34.
18. E.A. Lass, D.J. Sauza, D.C. Dunand D.N. Seidman: *Acta Mater.*, 2018, vol. 147, pp. 284–95.
19. T.M. Pollock, J. Dibbern, M. Tsunekane, J. Zhu, and A. Suzuki: *JOM*, 2010, vol. 62, pp. 58–63.
20. M.S. Titus, A. Suzuki, and T.M. Pollock: Superalloys, 2012, pp. 823–32.
21. H.Y. Yan, V.A. Vorontsov, and D. Dye: *Intermetallics*, 2014, vol. 48, pp. 44–53.
22. H.Y. Yan, V.A. Vorontsov, and D. Dye: *Corros. Sci.*, 2014, vol. 83, pp. 382–95.
23. C.H. Zenk, S. Neumeier, H.J. Stone, and M. Göken: *Intermetallics*, 2014, vol. 55, pp. 28–39.
24. S.K. Makineni, B. Nithin, and K. Chattopadhyay: *Acta Mater.*, 2015, vol. 85, pp. 85–94.
25. S.K. Makineni, A. Samanta, T. Rojhirunsakool, T. Alam, B. Nithin, A.K. Singh, R. Banerjee, and K. Chattopadhyay: *Acta Mater.*, 2015, vol. 97, pp. 29–40.
26. B. Nithin, A. Samanta, S.K. Makineni, T. Alam, P. Pandey, A.K. Singh, R. Banerjee, and K. Chattopadhyay: *J. Mater. Sci.*, 2017, vol. 52, pp. 11036–47.
27. P. Pandey, S.K. Makineni, A.Samanta, A.Sharma, S.M. Das, C. Srivastava, B. Gault, D. Raabe, A.K, Singh, and K. Chattopadhyay, Under Prep., 2017.
28. A.N. Behera, A. Chaudhuri, R. Kapoor, J.K. Chakravartty, and S. Suwas: *Mater. Des.*, 2016, vol. 92, pp. 750–59.
29. R. Kapoor, J.K. Chakravartty, C.C. Gupta, and S.L. Wadekar: *Mater. Sci. Eng. A.*, 2005, vol. 392, pp. 191–202.
30. S. Roy and S. Suwas: *J. Alloys Compd.*, 2013, vol. 548, pp. 110–25.
31. R. Kapoor and J.K. Chakravartty: *J. Nucl. Mater.*, 2002, vol. 306, pp. 126–33.
32. R. Kapoor, A.N. Behera, A. Sarkar, and J.K. Chakravartty: BARC Newsletter, 2015.
33. A.N. Behera, R. Kapoor, B. Paul, and J.K. Chakravartty: *Mater. Charact.*, 2017, vol. 126, pp. 135–45.

34. Y.V.R.K. Prasad, H.L. Gegel, S.M. Doraivelu, J.C. Malas, J.T. Morgan K.A. Lark D.R. Barker : *Metall. Trans. A.*, 1984, vol. 15, pp. 1883–92.
35. S. Venugopal and S.L. Mannan: *Mater. Sci. Eng. A.*, 1994, vol. 177, pp. 143–49.
36. Y.V.R.K. Prasad and S. Sasidhara: *Hot Working Guide: Compendium of Processing Maps*, ASM International, Materials Park, OH, 1997.
37. I. Ika Kartika H. Matsumoto A. Chiba : *Chiba Metall. Mater. Trans. A.*, 2009, vol. 40, pp. 1457–68.
38. V.A. Kumar, R.K. Gupta, S.V.S.N. Murty, and A. Durga: *J. Alloys Compd.*, 2016, vol. 676, pp. 527–41.
39. A. Chiba, S. Lee, H. Matsumoto, and M. Nakamura: *Mater. Sci. Eng. A.*, 2009, vol. 514, pp. 286–93.
40. T. Sakai: *J. Mater. Process. Technol.*, 1995, vol. 53, pp. 349–61.
41. H. Jiang, J. Dong, M. Zhang, L. Zheng, and Z. Yao: *J. Alloys Compd.*, 2015, vol. 647, pp. 338–50.
42. C.M. Sellars and W.J. Mctegart: *Acta Mater.*, 1966, vol. 14, pp. 1136–38.
43. H.Y. Wu, F.J. Zhu, S.C. Wang, W.R. Wang, C.C. Wang, and C.H. Chiu: *J. Mater. Sci.*, 2012, vol. 47, pp. 3971–81.
44. H.J. Mcqueen and N.D. Ryan: *Mater. Sci. Eng. A.*, 2002, vol. 322, pp. 43–63.
45. B. Paul, R. Kapoor, J.K. Chakravartty, A.C. Bidaye, I.G. Sharma, and A.K. Suri: *Scr. Mater.*, 2009, vol. 60, pp. 104–07.
46. S.S. Satheesh Kumar, T.R. Pinaki, and P.B.G. Appa: *J. Mater. Sci.*, 2015, vol. 50, pp. 6444–56.
47. H. Monajati, M. Jahazi, and A.K. Taheri: *Metall. Mater. Trans. A.*, 2005, vol. 36, pp. 895–905.
48. H. Ziegler: *Progress in Solid Mechanics*, 1963, pp. 63–193.
49. P.C.J. Gallagher: *Metall. Trans. A*, 1970, vol. 1, pp. 2429–61.
50. D. Li, Q. Guo, S. Guo, H. Peng, and Z. Wu: *Mater. Des.*, 2011, vol. 32, pp. 696–705.
51. S. Mitsche, C. Sommitsch, D. Huber, M. Stockinger, and P. Poelt: *Mater. Forum.*, 2012, vol. 709, pp. 2440–45.
52. G.R. Ebrahimi, A. Momeni, M. Jahazi, and P. Bocher: *Metall. Mater. Trans. A.*, 2014, vol. 45, pp. 2219–31.
53. L. Wang, F. Liu, J.J. Cheng, Q. Zuo, and C.F. Chen: *J. Alloys Compd.*, 2015, vol. 623, pp. 69–78.
54. Y. Wu, M. Zhang, X. Xie, J. Dong, and F. Lin: *J. Alloys Compd.*, 2016, vol. 656, pp. 119–31.
55. F.L. Sui, L.X. Xu, L.Q. Chen, and X.H. Liu: *J. Mater. Process. Technol.*, 2011, vol. 211, pp. 433–40.
56. I. Kartika, Y. Li, H. Matsumoto, and A. Chiba: *Mater. Trans.*, 2009, vol. 50, pp. 2277–84.
57. P.K. Chaudhury D. Zhao : *Atlas Form. Haynes*, 1993, vol. 188, pp. 1–64.
58. S. Guo, D. Li, H. Pen, Q. Guo, and J. Hu: *J. Nucl. Mater.*, 2011, vol. 410, pp. 52–58.
59. V.M. Sample, G.L. Fitzsimonss, and A.J. Deardo: *Acta Mater.*, 1987, vol. 35, pp. 367–79.